PCCP

PAPER

View Article Online
View Journal | View Issue

Cite this: *Phys. Chem. Chem. Phys.*, 2020, **22**, 556

Antiferromagnetic topological insulator $MnBi_2Te_4$: synthesis and magnetic properties†

Hao Li,‡[ab] Shengsheng Liu,‡[acde] Chang Liu,[f] Jinsong Zhang,[f] Yong Xu,[f] Rong Yu,[acde] Yang Wu,*[bg] Yuegang Zhang*[bf] and Shoushan Fan[bf]

Received 17th October 2019,
Accepted 4th December 2019

DOI: 10.1039/c9cp05634c

rsc.li/pccp

Recently, $MnBi_2Te_4$ has been discovered as the first intrinsic antiferromagnetic topological insulator (AFM TI), and it will become a promising material to discover exotic topological quantum phenomena. In this work, we have realized the successful synthesis of high-quality $MnBi_2Te_4$ single crystals by solid-state reactions. The as-grown $MnBi_2Te_4$ single crystal exhibits a van der Waals layered structure, which is composed of septuple Te–Bi–Te–Mn–Te–Bi–Te sequences as determined by X-ray diffraction and high-resolution high-angle annular dark field scanning transmission electron microscopy (HAADF-STEM). The magnetic order below 25 K as a consequence of A-type antiferromagnetic interaction between Mn layers in the $MnBi_2Te_4$ crystal suggests the unique interplay between antiferromagnetism and topological quantum states. Moreover, the transport measurements of $MnBi_2Te_4$ single crystals further confirm its magnetic transition. This study on the first AFM TI of $MnBi_2Te_4$ will guide the future research on other potential candidates in the MBi_xTe_y family (M = Ni, V, Ti, *etc.*).

Introduction

During the last decade, tremendous efforts and breakthroughs in topological quantum states have aroused great enthusiasm in pursuing the correlation between topology and symmetry.[1,2] The magnetism and crystal symmetry that affect the time reversal and inversion symmetry, respectively, are undoubtedly critical factors for condensed matter and thus have been deeply investigated in both theoretical and experimental aspects, resulting in numerous novel topological quantum phenomena.[1–13] From the perspective of materials science, it is of crucial importance to develop material systems with the coexistence of magnetism and topology that spontaneously breaks the time-reversal symmetry. Most current works tried to introduce magnetism into topological materials extrinsically by doping magnetic impurities.[14–19] However, the extrinsic magnetic defects are difficult to control experimentally, which hinders the progress in subsequent applications, for instance, dissipationless electric transportation in quantum anomalous Hall devices and topological quantum computation.[1,2] Hence, synthesizing novel intrinsic magnetic topological materials in which magnetism and topology natively coexist becomes a key research topic for future applications.

Appealingly, recent first-principle predictions and experiments have demonstrated $MnBi_2Te_4$ to be an intrinsic magnetic topological material, which belongs to antiferromagnetic (AFM) TIs and hosts unparalleled topological physics in both bulk and thin film form.[20–26] $MnBi_2Te_4$ crystalizes in the tetradymite-type structure with the $R\bar{3}m$ space group and lattice constants a = 4.33 Å and c = 40.91 Å.[27–29] As a member of the van der Waals (vdW) layered materials, $MnBi_2Te_4$ consists of Te–Bi–Te–Mn–Te–Bi–Te septuple layers (SLs) stacking in an ABC sequence along the c-axis (out-of-plane axis), as depicted in Fig. 1a. Therefore, it can be viewed as a derivative of the topological insulator Bi_2Te_3 by inserting a Mn–Te layer into the middle of its Te–Bi–Te–Bi–Te quintuple layer (QL). Each Mn^{2+} in high-spin configuration affords a 5 μ_B magnetic moment according to Hund's rule. The intralayer exchange coupling between Mn–Mn is ferromagnetic (FM) along an out-of-plane easy axis, while the interlayer exchange coupling between neighboring SLs is antiferromagnetic (AFM), generating a three-dimensional A-type AFM order.[21–26]

Hence, the synthesis of high-quality $MnBi_2Te_4$ single crystals with a well-defined AFM order is essential to the research of magnetic topological materials, as well as potential applications, such as dissipationless transport and low-power electronics.

[a] *School of Materials Science and Engineering, Tsinghua University, Beijing, 100084, P. R. China*
[b] *Tsinghua-Foxconn Nanotechnology Research Center, Tsinghua University, Beijing, 100084, P. R. China*
[c] *National Center for Electron Microscopy in Beijing, School of Materials Science and Engineering, Tsinghua University, Beijing, 100084, P. R. China*
[d] *Key Laboratory of Advanced Materials of Ministry of Education of China, Tsinghua University, Beijing, 100084, P. R. China*
[e] *State Key Laboratory of New Ceramics and Fine Processing, Tsinghua University, Beijing 100084, P. R. China*
[f] *State Key Laboratory of Low Dimensional Quantum Physics and Department of Physics, Tsinghua University, Beijing 100084, P. R. China. E-mail: yuegang.zhang@tsinghua.edu.cn*
[g] *Department of Mechanical Engineering, Tsinghua University, Beijing, 100084, P. R. China. E-mail: wuyangthu@tsinghua.edu.cn*

† Electronic supplementary information (ESI) available. See DOI: 10.1039/c9cp05634c

‡ These authors contributed equally to this work.

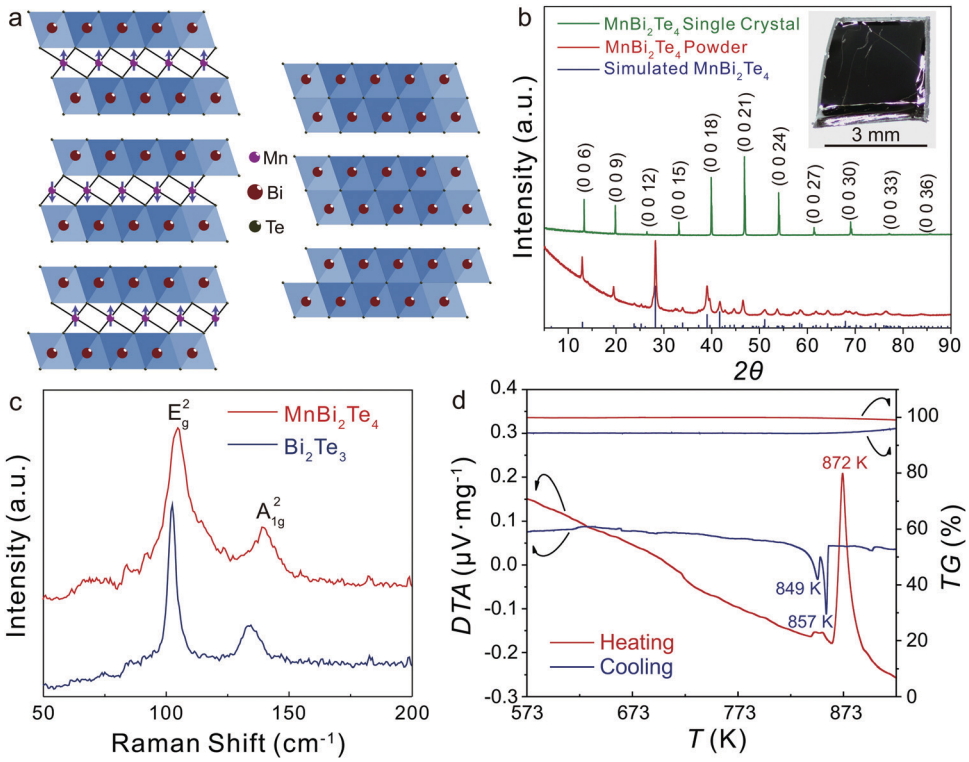

Fig. 1 (a) Schematic of crystal structure of the (1 1 0) crystallographic plane of $MnBi_2Te_4$ (left) and Bi_2Te_3 (right). The arrows denote the magnetic moment directions of Mn ions. (b) PXRD patterns of $MnBi_2Te_4$ single crystal (top) and powder (down). Inset: An optical image of the as-grown $MnBi_2Te_4$ single crystal. (c) Raman spectra of $MnBi_2Te_4$ and Bi_2Te_3. (d) Differential thermal analysis (DTA) and thermogravimetric (TG) analysis curves for $MnBi_2Te_4$.

According to previous studies, $MnBi_2Te_4$ can be synthesized through a number of approaches, but there is a lack of evidence for high purity crystalline samples.[28] During the preparation of this paper, we noticed that there have been several publications concerning the growth and characterization of $MnBi_2Te_4$ crystals.[22,27,29] However, the synthetic strategy toward high-quality millimeter-sized $MnBi_2Te_4$ single crystals with an unambiguous AFM transition is still challenging. More importantly, the oxidation behavior, which is critical to clarify the stability of exfoliated samples, has not been studied yet.

Herein, we report the effective synthesis of exclusive $MnBi_2Te_4$ single crystals with a clear and complete antiferromagnetic transition at 25 K. This progress could extend to a variety of potential AFM TIs in MBi_xTe_y (M = Ni, V, Ti, *etc.*).[26] The quality of the $MnBi_2Te_4$ single crystals is verified by a number of characterization techniques in detail. The oxidization behavior of $MnBi_2Te_4$ suggests that the surface of $MnBi_2Te_4$ tends to be oxidized in air while the bulk is stable. Intriguingly, magnetic and transport properties of $MnBi_2Te_4$ single crystals corroborate its AFM order and field-induced magnetic transitions, in good consistence with its prospective intrinsic AFM TI nature.

Results and discussion

Crystal growth and growth mechanism

The challenge in synthesizing ternary intermetallic compounds *via* solid-state approaches is how to circumvent the uneven distribution of elements in the reaction. To begin with, high-quality Bi_2Te_3 and MnTe binary were synthesized as precursors by directly reacting a stoichiometric mixture of high-purity Bi and Te, and Mn and Te, respectively (seen Synthesis and Fig. S1a, b, ESI†). Afterwards, the high-quality $MnBi_2Te_4$ single crystal was grown from a 1 : 1 mixture of Bi_2Te_3 and MnTe. The sample sealed in an evacuated silica ampoule was first heated to 973 K and slowly cooled to 864 K in 7 days, followed by prolonged annealing at 864 K for at least 14 days. After being air-quenched, shiny crystals were selected by cracking the sample chunk. The coarse part of the crystal was carefully cut-off with a scalpel or cleaned off using scotch tape with the aid of an optical microscope. The growth method can successfully afford $MnBi_2Te_4$ plate-like single crystals up to 3 mm in size with a shiny flat surface, indicating their layered structure (*cf.* inset of Fig. 1b).

In fact, attempts to directly react Bi, Mn and Te elements (seen Synthesis, trial 1) always gave Bi_2Te_3 and MnTe as impurities (product 1), which is confirmed by the powder X-ray diffraction (PXRD) results shown in Fig. S1c (ESI†). It is reasonable to assume that $MnBi_2Te_4$ forms by the solid-state intercalation of MnTe into Bi_2Te_3, which is favored upon long-term annealing. The short-term annealing yields a mixture of $MnBi_2Te_4$, Bi_2Te_3 and MnTe (product 2), which is revealed by the PXRD results shown in Fig. S1d (ESI†). Furthermore, to gain insights into the reaction mechanism, high-resolution high-angle annular dark field scanning transmission electron microscopy (HAADF-STEM) was performed on the (0 1 0) crystallographic plane of product 2, and it directly

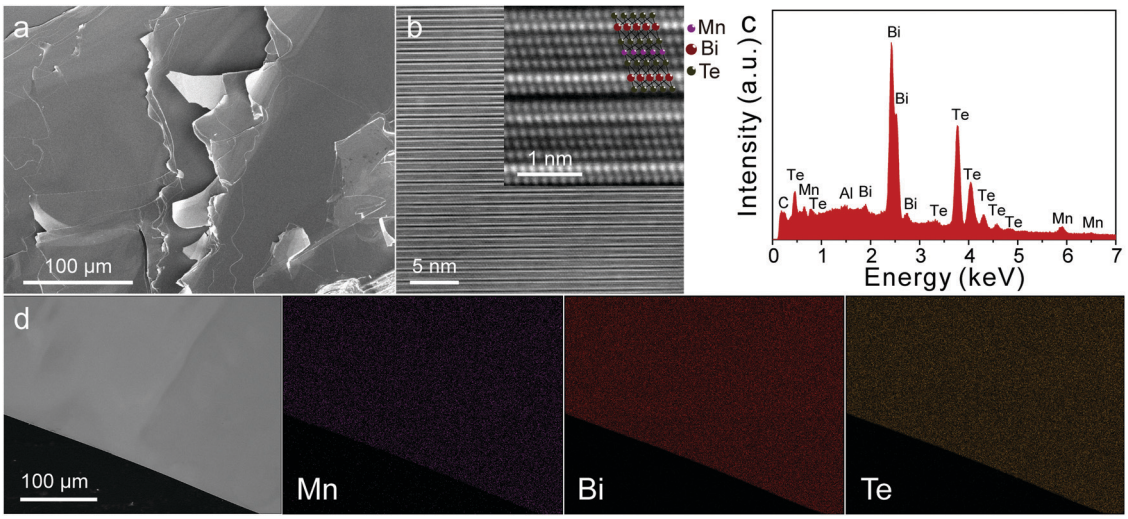

Fig. 2 (a) SEM image of exfoliated $MnBi_2Te_4$ single crystal. (b) HAADF-STEM image for the cross section of $MnBi_2Te_4$, in which SLs can be clearly resolved. Inset: Enlarged HAADF-STEM image superimposed with the schematic structure of $MnBi_2Te_4$. (c) EDX spectrum of $MnBi_2Te_4$ in (a). (d) SEM image and the corresponding EDX elemental mapping (Bi, Mn and Te).

shows the mixing of QLs from Bi_2Te_3 and SLs from $MnBi_2Te_4$ (Fig. S2, ESI†). This demonstrates an uncompleted reaction of Bi_2Te_3 and MnTe, which supports the aforementioned mechanism. In contrast, for the crystal obtained from prolonged annealing, the HAADF-STEM image in Fig. 2b clearly resolves its crystallographic plane with pure SLs from $MnBi_2Te_4$. Therefore, prolonged annealing is essential to guarantee the thorough intercalation of MnTe into Bi_2Te_3. The thermal property of $MnBi_2Te_4$ was revealed using differential thermal analysis (DTA). The as-grown $MnBi_2Te_4$ crystals display an intense exothermic peak at 872 K on the heating trace, indicating their melting point. Two endothermic peaks at 857 K and 849 K on the cooling run correspond to the crystallization of $MnBi_2Te_4$ and Bi_2Te_3, respectively. The lower intensity of the endothermic peaks compared to that of the exothermic peaks indicates that the crystallization of $MnBi_2Te_4$ is slow and difficult and $MnBi_2Te_4$ might be partly decomposed to Bi_2Te_3 above the melting point. The weight loss of $MnBi_2Te_4$ in the thermogravimetric (TG) curve (Fig. 1d) could result from the volatilization of Bi_2Te_3. As a result, the annealing temperature requires strict control to avoid material loss during the crystallization of $MnBi_2Te_4$.

Characterization

PXRD was carried out to determine the phase and quality of the as-grown $MnBi_2Te_4$ single crystal. Fig. 1b shows that the diffraction of raw $MnBi_2Te_4$ single crystals only occurs in the sharp and intense peaks that follow the (0 0 l), $l = 3n$, diffraction rule, verifying the rhombohedral symmetry and preferred orientation along the [0 0 1] direction. The PXRD pattern of finely ground $MnBi_2Te_4$ powder in Fig. 1b is in good agreement with the calculated PXRD pattern of $MnBi_2Te_4$, demonstrating its $R\bar{3}m$ space group and lattice constants a = 4.33 Å and c = 40.91 Å.[28,29] No impurity peaks are observed, confirming the high purity of the as-grown $MnBi_2Te_4$ single crystal. Besides, Fig. 1c shows the Raman spectrum of $MnBi_2Te_4$ single crystals with an appreciable blue shift with respect to that of Bi_2Te_3, which might result from the stronger in-plane bonding of Mn–Te.

The weak vdW interactions in the layered structure suggest that the top surface of $MnBi_2Te_4$ can be peeled off with scotch tape to expose fresh surface for the following characterization. Fig. 2a displays the scanning electron microscope (SEM) image of an exfoliated $MnBi_2Te_4$ single crystal with obviously segregated layers, confirming that $MnBi_2Te_4$ is a layered material integrated by van der Waals forces. Energy dispersive X-ray (EDX) spectroscopy was also used to analyze the element distribution of $MnBi_2Te_4$ crystals. As shown in Fig. 2c, no peaks other than Mn, Bi, Te, C and Al are observed in the EDX spectrum of $MnBi_2Te_4$. Please note that the presence of C and Al is attributed to the conductive tape and sample stage, respectively. Besides, the EDX elemental mapping reveals a uniform element distribution of Bi, Mn and Te (Fig. 2d). The element ratio is further confirmed by inductively coupled plasma mass spectrometry (ICP-MS) analysis, which showed that Mn : Bi : Te is 1 : 2.14 : 3.96, agreeing with the chemical formula of the title compound. More importantly, the HAADF-STEM image in Fig. 2b clearly shows the cross section of the as-grown $MnBi_2Te_4$ single crystal with unambiguously resolved SLs. As the contrast is proportional to the atomic number, the relatively dark atomic layer in the middle of SLs can be assigned to Mn, while the two brightest layers are from Bi atoms and the other three layers of medium brightness are from Te. Thus, the HAADF-STEM study verifies the stacking sequence of Te–Bi–Te–Mn–Te–Bi–Te in a SL, which agrees well with the structure model.

Oxidization behavior and stability

We conducted X-ray photoelectron spectroscopy (XPS) measurements to gain insights into the oxidation states of $MnBi_2Te_4$. The XPS measurement was firstly carried out on the fresh surface of the $MnBi_2Te_4$ crystal. The XPS survey spectrum verified the elemental composition (Fig. S3a, ESI†). A low O 1s peak indicates slight surface oxidation of $MnBi_2Te_4$ due to the short exposure to the

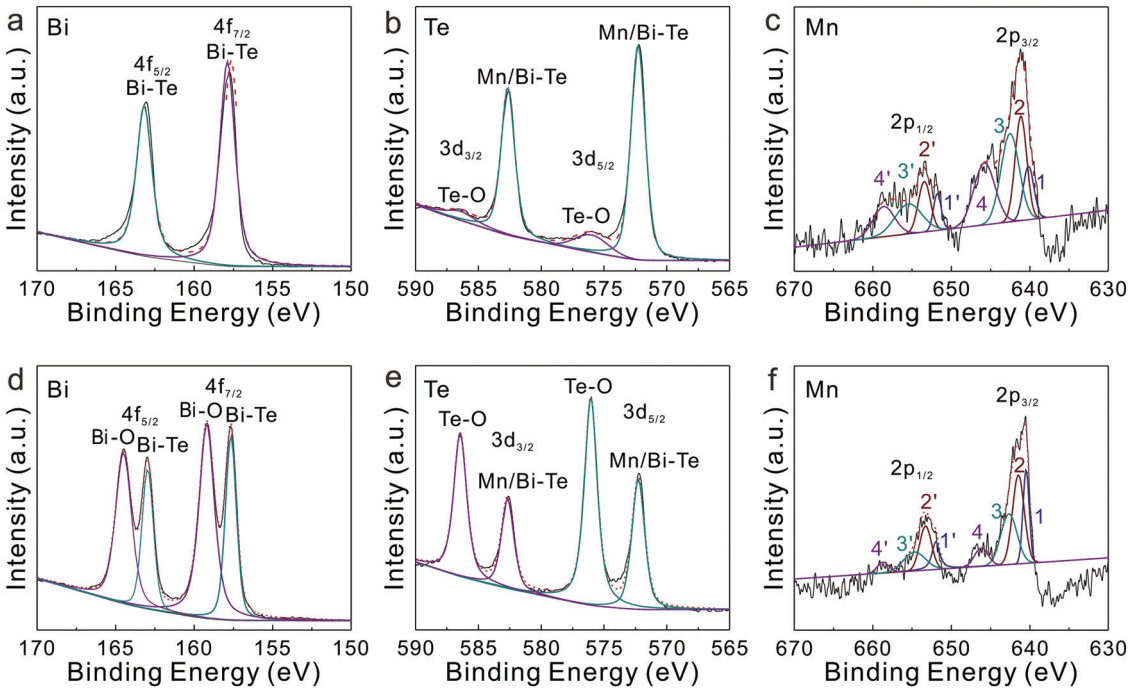

Fig. 3 High-resolution XPS spectra of fresh (a–c) and oxidized (d–f) surface of $MnBi_2Te_4$, respectively. (a and d) Bi 4f, (b and e) Te 3d and (c and f) Mn 2p spectra.

atmosphere during sample transfer. Furthermore, the oxidation states for each element can be assigned in the corresponding high-resolution spectra in Fig. 3a–c. Two peaks in the Bi 4f spectrum at 157.8 eV and 163.1 eV are ascribed to Bi $4f_{7/2}$ and Bi $4f_{5/2}$ of Bi^{3+} in Bi–Te bonds (Fig. 3a).[30–32] As shown in Fig. 3b, the Te 3d spectrum contains two major peaks at 572.2 eV (Te $3d_{5/2}$) and 582.6 eV (Te $3d_{3/2}$), corresponding to Te^{2-} in Bi–Te bonds and Mn–Te bonds.[32,33] In addition, two minor peaks at 576.0 eV and 586.3 eV can be observed in the Te 3d spectrum, which are attributed to Te–O bonds and indicate slight oxidation of the $MnBi_2Te_4$ surface.[30] Fig. 3c displays the Mn 2p spectrum, which can be deconvoluted into two sets of four sub peaks (Mn1(′), Mn2(′), Mn3(′), and Mn4(′)). Mn1 and Mn1′ peaks are located at 640.1 eV and 651.8 eV, which arise from broken Mn–Te bonds caused by oxidation. The strongest Mn2 and Mn2′ peaks at 641.1 eV and 653.4 eV are due to Mn^{2+} in Mn–Te bonds, indicating the major oxidation state of Mn is 2+. Mn3 and Mn3′ at 642.5 eV and 655.5 eV, and Mn4 and Mn4′ at 645.8 eV and 658.6 eV are satellite peaks of Mn1 and Mn1′, and Mn2 and Mn2′, respectively, and they result from the charge transfer between the outer shell of Te and the unfilled 3d shell of Mn in the photoelectron process.[33–36] To reveal the oxidation stability, we exposed the $MnBi_2Te_4$ single crystal to air over a week, and then investigated its oxidation states using XPS. The survey spectrum in Fig. S3b (ESI†) shows an evidently higher O 1s peak, indicating the more severe oxidation owing to the longer exposure to air. This was also proved by high-resolution XPS spectra. The Bi 4f spectrum in Fig. 3d exhibits two strong peaks at 159.2 eV and 164.4 eV that can be assigned to the Bi–O bonds.[30] Similarly, Te 3d (Fig. 3e) and Mn 2p (Fig. 3f) spectra of the oxidized $MnBi_2Te_4$ surface display more pronounced oxidation peaks (Te–O) and peaks arising from oxidation (Mn1 and Mn1′) than those of the fresh $MnBi_2Te_4$ surface. Interestingly, EDX and Raman results of oxidized $MnBi_2Te_4$ in Fig. S4 (ESI†) show no obvious difference from those of fresh $MnBi_2Te_4$, implying that the oxidation is a surface behavior of $MnBi_2Te_4$. Therefore, we can conclude that the surface of $MnBi_2Te_4$ is likely to be oxidized and it is critical to keep samples in an inert atmosphere, especially when handling exfoliated few-layer $MnBi_2Te_4$ samples.

Magnetic and transport properties

Magnetic properties of the as-grown $MnBi_2Te_4$ single crystal were inspected using a superconducting quantum interference device (SQUID) under a zero-field-cooled (ZFC) process. Fig. 4a and b display the temperature dependence of magnetic susceptibility (χ) for the $MnBi_2Te_4$ single crystal in out-of-plane ($\boldsymbol{H}//c$) and in-plane ($\boldsymbol{H}//ab$) magnetic fields, respectively. As displayed in Fig. 4a, the magnetic susceptibility of $MnBi_2Te_4$ in $\boldsymbol{H}//c$ increases as temperature decreases and reaches a maximum at 25 K, and then it begins to decrease dramatically. This AFM transition corresponds to AFM order originating from exchange coupling between Mn^{2+} in the neighboring SLs and displays a Néel temperature (T_N) of 25 K, which is in good consistence with previous reports.[22,27,29] Noticeably, the magnetic susceptibility approaches zero as the $MnBi_2Te_4$ crystal is cooled down to 2 K, implying an ideal antiferromagnetic state with an out-of-plane easy axis. However, the Néel transition tends to become weaker and finally disappears as the applied out-of-plane magnetic field increases, due to the suppression and spin-flop of interlayer antiferromagnetic coupling caused by an external out-of-plane magnetic field.[27] The decrease of T_N

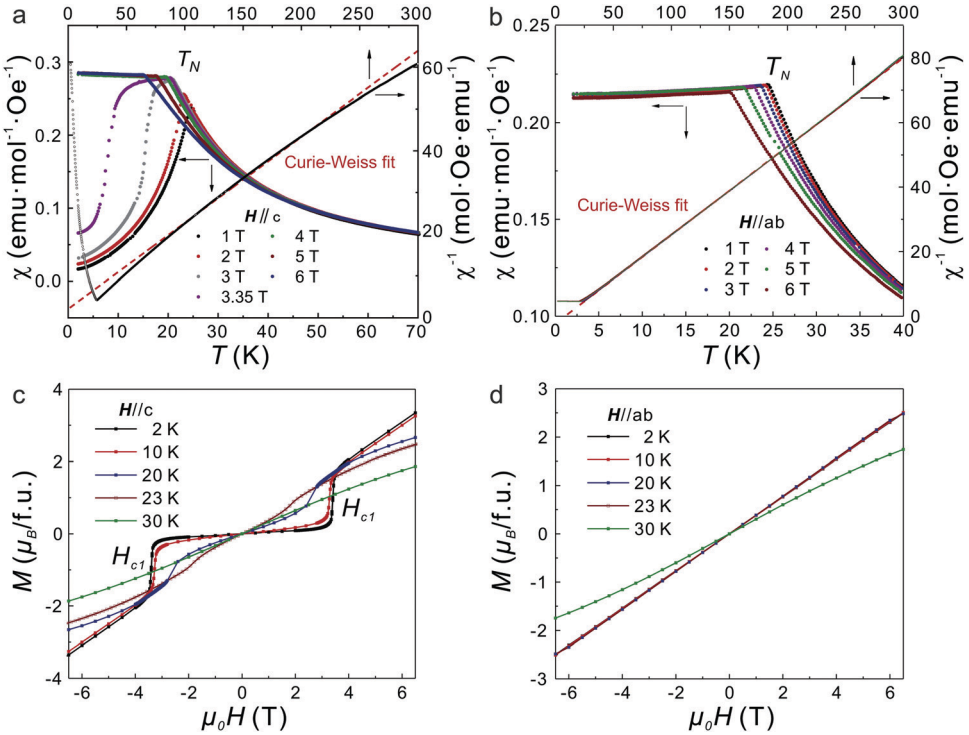

Fig. 4 Magnetic properties of $MnBi_2Te_4$ single crystal. (a and b) Temperature dependence of magnetic susceptibility for the $MnBi_2Te_4$ single crystal measured under ZFC and inverse magnetic susceptibility as a function of temperature (top *x* axis and right *y* axis). The symbol and dash line represent the experimental data and Curie–Weiss fit. Magnetic field is out-of-plane (a) and in-plane (b), respectively. (c and d) Field dependence of magnetization for the $MnBi_2Te_4$ crystal measured at different temperatures. Magnetic field is out-of-plane (c) and in-plane (d), respectively.

with increasing applied magnetic field in Fig. S5 (ESI†) also manifests the suppression of magnetic order. The inverse magnetic susceptibility above T_N shows a linear dependence of temperature above T_N, which follows the Curie–Weiss (CW) law $\chi = C/(T + \theta_{CW})$. The linear fitting of χ^{-1} *versus* T provides a positive CW temperature $\theta_{CW} \sim 10$ K, and an effective magnetic moment of $\mu_{eff}^{c} \sim 6.2\ \mu_B$ by taking the relationship $C = N_A\mu_{eff}^2/3k_B$ into account. This value agrees with the spin-only μ_{eff} of 5.92 μ_B for high-spin Mn^{2+} ions with a $3d^5$ configuration, where $\mu_{eff} = 2\sqrt{J(J+1)}\ \mu_B$, $J = 5/2$. Comparing with the recently published results, it excels over the previously reported magnetic moment of 4.04(13) μ_B per Mn from neutron diffraction,[27] and is similar to $\mu_{eff} = 5.9(1)\ \mu_B$ from magnetic measurements.[29] The consistency between measured and calculated μ_{eff} could originate from the complete intercalation of Mn–Te bilayers into the Bi_2Te_3 QLs in this long-term synthesis strategy. We also note that the deviation from the CW law near T_N possibly arises from strong spin fluctuations induced by magnetic phase transition. Regarding measurements in ***H*//*ab***, the inverse magnetic susceptibility (Fig. 4b) also follows the CW law and provides an effective magnetic moment of $\mu_{eff}^{ab} \sim 5.4\ \mu_B$, which is close to the spin-only $\mu_{eff} \sim 5.92\ \mu_B$ for a free Mn^{2+} ion. In addition, we can extract a negative Curie–Weiss temperature of $\theta_{CW} \sim -8$ K, implying FM interactions among the Mn^{2+}, consistent with the predicted A-type AFM feature of $MnBi_2Te_4$. While the magnetic susceptibility decreases dramatically below T_N in ***H*//*c***, it only declines slightly below T_N in ***H*//*ab***. The obvious difference of the magnetic susceptibility between in-plane and out-of-plane directions suggests anisotropy of the AFM order.[25,37] This anisotropic AFM order of $MnBi_2Te_4$ is further revealed in the field dependence of magnetization in Fig. 4c and d, where the field dependence of magnetization in ***H*//*c*** and ***H*//*ab*** is displayed. The magnetization displays a linear dependence and shows no hint of saturation for $T > T_N$, indicating the paramagnetic state. In contrast, for ***H*//*c*** and $T < T_N$, *M*–*H* curves increase slowly as the field is increased from zero, and exhibit a sharp increase across a critical field, $\mu_0H_{c1} \sim 3.35$ T, and become linear for $\mu_0H > \mu_0H_{c1}$, suggesting a metamagnetic phase transition into a canted AFM state caused by field-induced suppression of magnetic order,[22,27] in good agreement with the χ–*T* curves. The obvious difference of the magnetic susceptibility between in-plane and out-of-plane directions suggests an anisotropic AFM order. For ***H*//*ab***, *M*–*H* curves almost overlap as $T < T_N$, suggesting a linear dependence and showing no obvious transition. This is consistent with the χ–*T* behavior in ***H*//*ab*** and further confirms the anisotropy of the AFM order. The magnetic anisotropy energy of bulk $MnBi_2Te_4$ has been calculated to be 0.225 meV per Mn.[25] Moreover, a recent report has discussed the magnetic anisotropy of monolayer $MnBi_2Te_4$ in which the exchange interaction in monolayer $MnBi_2Te_4$ is nearly isotropic and almost has no contribution to the magnetic anisotropy. The magnetic anisotropy originates from single-ion anisotropy, leading to a ferromagnetic Curie temperature of about 20 K.[37] Lastly, the absence of hysteresis in the *M*–*H* curves is consistent with the AFM state.

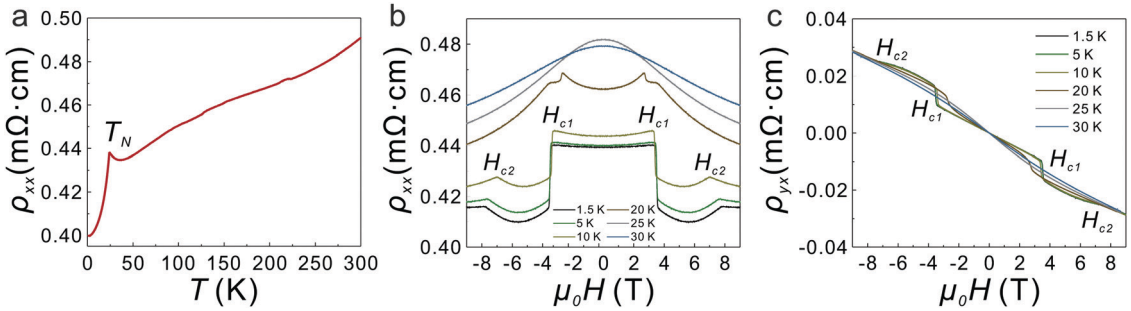

Fig. 5 Transport properties of $MnBi_2Te_4$ single crystal. (a) Temperature dependence of longitudinal resistivity ρ_{xx} measured from 1.6 K to room temperature. The sharp AFM transition is revealed near T_N = 25 K. (b) MR curves in an out-of-plane magnetic field at varied temperatures. The lower and upper critical fields (H_{c1} and H_{c2}) are labeled and the temperatures for MR curves are shown by different color from 30 K to 1.5 K. (c) Magnetic field dependence of Hall resistivity traces measured at the same temperatures.

Electrical transport measurements were carried out on a $MnBi_2Te_4$ single crystal with a thickness of ~10 μm. Fig. 5a displays the metallic temperature dependence of longitudinal resistivity ρ_{xx} from 1.5 K to room temperature. A sharp transition at ~25 K corresponding to the AFM transition is consistent with T_N from the magnetic property measurement. The magnetoresistivity (MR) curves measured in $\boldsymbol{H}//c$ at different temperatures are shown in Fig. 5b. As the magnetic field is increased from zero, a sharp decrease of ρ_{xx} takes place over the critical magnetic field (H_{c1}) below T_N, which indicates the metamagnetic phase transition consistent with the forenamed magnetic properties. When further increasing the magnetic field, a kink followed by a gradual decrease in ρ_{xx} emerges, suggesting that the fully polarized spin in Mn^{2+} occurs at a higher critical magnetic field (H_{c2}). The similar electric transport behavior with both critical magnetic fields H_{c1} and H_{c2} was also observed and reported in recent publications.[22,38,39] Fig. 5c shows the field dependence of Hall resistivity ρ_{yx} at the same temperatures. The negative slopes indicate that electron is the dominating charge carrier, possibly caused by defects such as Te deficiency, Bi redundancy or antisite disordering.[29] From the linear region of the Hall curves ($H < H_{c1}$), the electron density is extracted to be 2.3×10^{20} cm^{-3}, and the mobility is calculated to be ~630 cm^2 V^{-1} s^{-1} at 1.5 K, which agrees well with the electron density and mobility of $MnBi_2Te_4$ in recent reports.[22,38,39] Similarly, Hall curves exhibit a sharp change in the slope across H_{c1} and a twist across H_{c2} below T_N, which conforms to the sharp decrease and kink at H_{c1} and H_{c2} in ρ_{xx} (Fig. 5b), respectively.

Conclusions

In summary, we have developed a facile strategy to synthesize high-quality $MnBi_2Te_4$ single crystals by prolonged annealing across a narrow temperature window. The crystal structure and quality of $MnBi_2Te_4$, especially its septuple Te–Bi–Te–Mn–Te–Bi–Te sequences and oxidation behavior, have been revealed *via* various characterization techniques. The as-grown $MnBi_2Te_4$ single crystal exhibits an evident AFM transition at 25 K and field-induced magnetic transitions in both magnetic and transport properties, manifesting its intrinsic and anisotropic AFM nature. This study on the first AFM TI of $MnBi_2Te_4$ could open an avenue to novel quantum states and topological phenomena and further inspire research on other potential AFM TIs of MBi_xTe_y (M = Cr, V, Ti, *etc.*).[26]

Experimental

Materials

Bi (99.99%, Adamas), Mn (99.95%, Alfa Aesar) and Te (99.999%, Aladdin) were used as received.

Synthesis

Synthesis of MnTe. Polycrystalline MnTe was synthesized by directly heating a stoichiometric mixture of high-purity Mn and Te at 1273 K in a vacuum-sealed silica ampoule for 3 days.

Synthesis of Bi_2Te_3. Bi_2Te_3 crystal was synthesized by a direct solid-state reaction of a stoichiometric mixture of high-purity Bi and Te. The reaction mixture was vacuum-sealed in a silica ampoule, and heated to 1083 K and held for 24 h. After being slowly cooled to 833 K at a rate of 0.1 K min^{-1}, the ampoule was quenched in air to obtain the Bi_2Te_3 crystal.

Trial 1. The product 1 was synthesized by direct heating of a stoichiometric mixture of high-purity Mn, Bi and Te at 973 K in a vacuum-sealed silica ampoule for 24 h.

Characterization

The powder X-ray diffraction (PXRD) patterns were collected on a PANalytical Empyrean X-ray diffractometer, using Cu Kα radiation and operating at 45 kV and 40 mA.

Differential thermal analysis (DTA) and thermogravimetric (TG) analysis were carried out using a NETZSCH STA449 F3 simultaneous thermal analyzer under N_2 atmosphere. The $MnBi_2Te_4$ single crystal sample was enclosed in an Al_2O_3 crucible, and heated from room temperature to 953 K at a rate of 10 K min^{-1} and then cooled to 573 K at a rate of 3 K min^{-1}.

Raman spectra were collected using a Horiba Jobin Yvon LabRam-HR/VV Spectrometer with a 514 nm laser source and a grating with 1800 lines per millimeter.

Chemical analysis was carried out using a Thermo Fisher iCP QC inductively coupled plasma mass spectrometer (ICP-MS),

after dissolution of the $MnBi_2Te_4$ single crystal sample in aqua regia.

Morphology and element analyses of $MnBi_2Te_4$ crystals were carried out using a FEI NOVA SEM450 scanning electron microscope (SEM) equipped with an energy dispersive X-ray (EDX) detector.

HAADF-STEM images were collected using a Titan Cubed Themis G2 300 Double Aberration-Corrected Transmission Electron Microscope operating at 300 kV, while the $MnBi_2Te_4$ single crystal sample for cross-sectional observation was prepared *via* a Zeiss Auriga focused ion beam (FIB) instrument using SiO_2 as a protective layer.

X-ray photoelectron spectroscopy

Measurements were performed using an Ulvac-Phi Quantera II X-ray photoelectron spectrometer with monochromatic Al Kα radiation (1486.6 eV). The carbon 1s peak at 284.8 eV is used as the reference.

Magnetic property

Measurements were carried out using a Quantum Design Superconducting Quantum Interference device using a vibrating sample magnetometer using a raw $MnBi_2Te_4$ single crystal sample.

Transport property

Measurements were carried out using a cryostat (Oxford Instruments) with a base temperature of $\sim$1.5 K and a magnetic field up to 9 T. The longitudinal and Hall voltages were detected simultaneously by using Stanford Research Instrument SR830 lock-in amplifiers with an AC current generated with a Keithley 6221 current source. The $MnBi_2Te_4$ single crystal sample with a thickness of $\sim$10 μm was obtained by mechanical exfoliation of a raw $MnBi_2Te_4$ single crystal using scotch tape.

Conflicts of interest

There are no conflicts to declare.

Acknowledgements

This work was supported by the Basic Science Center Project of NSFC (Grant No. 51788104), the Ministry of Science and Technology of China (Grants No. 2018YFA0307100, and No. 2018YFA0305603), and the National Natural Science Foundation of China (Grant No. 11674188, 21975140, 51991343, U1832218).

References

1 M. Z. Hasan and C. L. Kane, *Rev. Mod. Phys.*, 2010, **82**, 3045–3067.
2 X.-L. Qi and S.-C. Zhang, *Rev. Mod. Phys.*, 2011, **83**, 1057–1110.
3 N. P. Armitage, E. J. Mele and A. Vishwanath, *Rev. Mod. Phys.*, 2018, **90**, 015001.
4 F. D. M. Haldane, *Rev. Mod. Phys.*, 2017, **89**, 040502.
5 A. M. Essin, J. E. Moore and D. Vanderbilt, *Phys. Rev. Lett.*, 2009, **102**, 146805.
6 R. Yu, W. Zhang, H.-J. Zhang, S.-C. Zhang, X. Dai and Z. Fang, *Science*, 2010, **329**, 61–64.
7 L. Fu and C. L. Kane, *Phys. Rev. Lett.*, 2008, **100**, 096407.
8 E. Liu, Y. Sun, N. Kumar, L. Muchler, A. Sun, L. Jiao, S. Y. Yang, D. Liu, A. Liang, Q. Xu, J. Kroder, V. Suss, H. Borrmann, C. Shekhar, Z. Wang, C. Xi, W. Wang, W. Schnelle, S. Wirth, Y. Chen, S. T. B. Goennenwein and C. Felser, *Nat. Phys.*, 2018, **14**, 1125–1131.
9 P. Tang, Q. Zhou, G. Xu and S.-C. Zhang, *Nat. Phys.*, 2016, **12**, 1100–1104.
10 G. Xu, H. Weng, Z. Wang, X. Dai and Z. Fang, *Phys. Rev. Lett.*, 2011, **107**, 186806.
11 H. Zhang, Y. Xu, J. Wang, K. Chang and S.-C. Zhang, *Phys. Rev. Lett.*, 2014, **112**, 216803.
12 W. K. Tse and A. H. MacDonald, *Phys. Rev. Lett.*, 2010, **105**, 057401.
13 Q. L. He, L. Pan, A. L. Stern, E. C. Burks, X. Che, G. Yin, J. Wang, B. Lian, Q. Zhou, E. S. Choi, K. Murata, X. Kou, Z. Chen, T. Nie, Q. Shao, Y. Fan, S.-C. Zhang, K. Liu, J. Xia and K. L. Wang, *Science*, 2017, **357**, 294–299.
14 C. Z. Chang, W. Zhao, D. Y. Kim, H. Zhang, B. A. Assaf, D. Heiman, S. C. Zhang, C. Liu, M. H. Chan and J. S. Moodera, *Nat. Mater.*, 2015, **14**, 473–477.
15 C.-Z. Chang, J. Zhang, X. Feng, J. Shen, Z. Zhang, M. Guo, K. Li, Y. Ou, P. Wei, L.-L. Wang, Z.-Q. Ji, Y. Feng, S. Ji, X. Chen, J. Jia, X. Dai, Z. Fang, S.-C. Zhang, K. He, Y. Wang, L. Lu, X.-C. Ma and Q.-K. Xue, *Science*, 2013, **340**, 167–170.
16 F. Katmis, V. Lauter, F. S. Nogueira, B. A. Assaf, M. E. Jamer, P. Wei, B. Satpati, J. W. Freeland, I. Eremin, D. Heiman, P. Jarillo-Herrero and J. S. Moodera, *Nature*, 2016, **533**, 513–516.
17 M. Mogi, M. Kawamura, R. Yoshimi, A. Tsukazaki, Y. Kozuka, N. Shirakawa, K. S. Takahashi, M. Kawasaki and Y. Tokura, *Nat. Mater.*, 2017, **16**, 516–521.
18 D. Xiao, J. Jiang, J. H. Shin, W. Wang, F. Wang, Y. F. Zhao, C. Liu, W. Wu, M. H. W. Chan, N. Samarth and C. Z. Chang, *Phys. Rev. Lett.*, 2018, **120**, 056801.
19 M. Mogi, M. Kawamura, A. Tsukazaki, R. Yoshimi, K. S. Takahashi, M. Kawasaki and Y. Tokura, *Sci. Adv.*, 2017, **3**, eaao1669.
20 G. Yan, G. Jingwen, L. Jiaheng, Z. Kejing, L. Menghan, L. Xiaozhi, Z. Qinghua, G. Lin, T. Lin, F. Xiao, Z. Ding, L. Wei, S. Canli, W. Lili, P. Yu, C. Xi, W. Yayu, Y. Hong, D. Wenhui, X. Yong, Z. Shou-Cheng, M. Xucun, X. Qi-Kun and H. Ke, *Chin. Phys. Lett.*, 2019, **36**, 076801.
21 R. C. Vidal, H. Bentmann, T. R. F. Peixoto, A. Zeugner, S. Moser, C. H. Min, S. Schatz, K. Kißner, M. Unzelmann, C. I. Fornari, H. B. Vasili, M. Valvidares, K. Sakamoto, J. Fujii, I. Vobornik, T. K. Kim, R. J. Koch, C. Jozwiak, A. Bostwick, J. D. Denlinger, E. Rotenberg, J. Buck, M. Hoesch, F. Diekmann, S. Rohlf, M. Kallane, K. Rossnagel, M. M. Otrokov, E. V. Chulkov, M. Ruck, A. Isaeva and F. Reinert, arXiv:1903.11826v1, Cond-Mat, 2019.
22 S. H. Lee, Y. Zhu, Y. Wang, L. Miao, T. Pillsbury, S. Kempinger, D. Graf, N. Alem, C.-Z. Chang, N. Samarth and Z. Mao, arXiv:1812.00339, Cond-Mat, 2018.

23 D. Zhang, M. Shi, T. Zhu, D. Xing, H. Zhang and J. Wang, *Phys. Rev. Lett.*, 2019, **122**, 206401.
24 B. Chen, F. Fei, D. Zhang, B. Zhang, W. Liu, S. Zhang, P. Wang, B. Wei, Y. Zhang, J. Guo, Q. Liu, Z. Wang, X. Wu, J. Zong, X. Xie, W. Chen, Z. Sun, D. Shen, S. Wang, Y. Zhang, M. Zhang, F. Song, H. Zhang and B. Wang, arXiv:1903.09934, Cond-Mat, 2019.
25 M. M. Otrokov, I. P. Rusinov, M. Blanco-Rey, M. Hoffmann, A. Y. Vyazovskaya, S. V. Eremeev, A. Ernst, P. M. Echenique, A. Arnau and E. V. Chulkov, *Phys. Rev. Lett.*, 2019, **122**, 107202.
26 J. Li, Y. Li, S. Du, Z. Wang, B.-L. Gu, S.-C. Zhang, K. He, W. Duan and Y. Xu, *Sci. Adv.*, 2019, **5**, eaaw5685.
27 J. Q. Yan, Q. Zhang, T. Heitmann, Z. Huang, K. Y. Chen, J. G. Cheng, W. Wu, D. Vaknin, B. C. Sales and R. J. McQueeney, *Phys. Rev. Mater.*, 2019, **3**, 064202.
28 D. S. Lee, T.-H. Kim, C.-H. Park, C.-Y. Chung, Y. S. Lim, W.-S. Seo and H.-H. Park, *CrystEngComm*, 2013, **15**, 5532–5538.
29 A. Zeugner, F. Nietschke, A. U. B. Wolter, S. Gass, R. C. Vidal, T. R. F. Peixoto, D. Pohl, C. Damm, A. Lubk, R. Hentrich, S. K. Moser, C. Fornari, C. H. Min, S. Schatz, K. Kissner, M. Uenzelmann, M. Kaiser, F. Scaravaggi, B. Rellinghaus, K. Nielsch, C. Hess, B. Buechner, F. Reinert, H. Bentmann, O. Oeckler, T. Doert, M. Ruck and A. Isaeva, *Chem. Mater.*, 2019, **31**, 2795–2806.
30 H. Bando, K. Koizumi, Y. Oikawa, K. Daikohara, V. A. Kulbachinskii and H. Ozaki, *J. Phys.: Condens. Matter*, 2000, **12**, 5607–5616.
31 A. M. Vora, *Cryst. Res. Technol.*, 2007, **42**, 286–289.
32 J. Fu, S. Song, X. Zhang, F. Cao, L. Zhou, X. Li and H. Zhang, *CrystEngComm*, 2012, **14**, 2159–2165.
33 R. J. Iwanowski, M. H. Heinonen and B. Witkowska, *J. Alloys Compd.*, 2010, **491**, 13–17.
34 R. J. Iwanowski, M. H. Heinonen and E. Janik, *Chem. Phys. Lett.*, 2004, **387**, 110–115.
35 R. J. Iwanowski, M. H. Heinonen and E. Janik, *Appl. Surf. Sci.*, 2005, **249**, 222–230.
36 K. Woochul, P. Il Jin, K. Hyung Joon, L. Wooyoung, K. Sam Jin and K. Chul Sung, *IEEE Trans. Magn.*, 2009, **45**, 2424–2427.
37 Y. Li, Z. Jiang, J. Li, S. Xu and W. Duan, *Phys. Rev. B: Condens. Matter Mater. Phys.*, 2019, **100**, 134438.
38 Y. Deng, Y. Yu, M. Z. Shi, J. Wang, X. H. Chen and Y. Zhang, arXiv:1904.11468, Cond-Mat, 2019.
39 C. Liu, Y. Wang, H. Li, Y. Wu, Y. Li, J. Li, K. He, Y. Xu, J. Zhang and Y. Wang, arXiv:1905.00715, Cond-Mat, 2019.